nature communications

Article

https://doi.org/10.1038/s41467-025-58526-7

Origin of yield stress and mechanical plasticity in model biological tissues

Received: 14 August 2024

Accepted: 25 March 2025

Published online: 05 April 2025

Check for updates

Anh Q. Nguyen [1,2], Junxiang Huang [1,2] & Dapeng Bi [1,2]

During development and under normal physiological conditions, biological tissues are continuously subjected to substantial mechanical stresses. In response to large deformations, cells in a tissue must undergo multicellular rearrangements to maintain integrity and robustness. However, how these events are connected in time and space remains unknown. Here, using theoretical modeling, we study the mechanical plasticity of cell monolayers under large deformations. Our results suggest that the jamming-unjamming (solid-fluid) transition can vary significantly depending on the degree of deformation, implying that tissues are highly unconventional materials. We elucidate the origins of this behavior. We also demonstrate how large deformations are accommodated through a series of cellular rearrangements, similar to avalanches in non-living materials. We find that these 'tissue avalanches' are governed by stress redistribution and the spatial distribution of "soft" or vulnerable spots, which are more prone to undergo rearrangements. Finally, we propose a simple and experimentally accessible framework to infer tissue-level stress and predict avalanches based on static images.

During morphogenesis and under normal physiological conditions, biological tissues continuously experience substantial mechanical stresses[1]. Research efforts to understand the remarkable deformability of epithelial tissues employ both experimental and computational approaches. Experimentally, studies focus on the tissue's responses to external stresses[2–6], where a stress-driven unjamming transition has been noted[6]. On the simulation front, the cellular Potts and Vertex-based models are utilized to probe tissue rheology[7,8], uncovering nonlinear elasticity and rheological properties[8,9]. However, with few exceptions[10], research has predominantly focused on the shear startup regime. This leaves a gap in our understanding of tissue behavior under steady shear and the mechanisms underpinning yield-stress behavior in tissues. Beyond the yield stress, materials typically flow through plastic rearrangements. Similarly, within tissues, mechanical plasticity occurs through cellular rearrangements, enabling the maintenance of integrity and robustness. While there is extensive literature on how individual cells rearrange with their neighbors[11–14], significant gaps remain in understanding how these localized events connect over time and space. Moreover, a major challenge lies in elucidating how these collective interactions lead to mechanical responses at the tissue level. In the context of material plasticity, avalanche-like behavior, prevalent in phenomena ranging from earthquakes to ferromagnets, involves small perturbations triggering significant collective responses[15]. Systems exhibiting these instabilities display self-organized criticality[16] and power law scaling in their observables, indicating that the process belongs to a specific universality class. Proliferation-driven avalanche-like behavior has recently been studied using numerical simulation of the Drosophila eye disc, suggesting that avalanches provide a macroscopic mechanism for epithelial tissues to alleviate accumulated proliferative stress[17]. Additionally, there is evidence of motility-induced avalanches in the epithelial tissue of Trichoplax adhaerens[18], where dynamic forces from the organism's motility trigger localized microfractures that cascade into larger fractures, a hallmark of avalanche dynamics. Moreover, shear-induced avalanches were first documented in vertex-based models in[19] and later in[9,10], yet a detailed examination of the growth and evolution of these avalanches is still lacking.

[1]Department of Physics and, Northeastern University, Boston, MA, USA. [2]Center for Theoretical Biological Physics, Northeastern University, Boston, MA, USA. e-mail: d.bi@northeastern.edu

In this work, we investigate tissue mechanical plasticity using the Voronoi-based Vertex model under quasi-static shear. Our results imply that the solid-fluid transition point–also referred to as the jamming-unjamming transition in recent literature[20–22]–does not occur at a singular point but varies depending on the degree of shear deformation the tissue undergoes. Furthermore, we discover states where tissues possess yield-stress properties but lack a conventional shear modulus in our simulation. These states exist in a solid-fluid coexistence phase near the jamming-unjamming transition, which we explore through a modified version of the Soft Glassy Rheology model to elucidate the origins of these complex states. The coexistence of fluid and solid phases suggests that even traditionally fluid-like tissues can accumulate stress in response to deformation, highlighting the need for a parameter-free, model-independent tissue stress inference method. Here, we propose an easily implementable metric to estimate tissue stress from static snapshots of tissue configurations without requiring any prior knowledge of the system. Additionally, our research not only provides insight to how tissue manages large deformations through multicellular rearrangements akin to avalanches observed in non-living materials but also connects these phenomena to the tissue-level mechanical responses discussed earlier. These "tissue avalanches" are driven by stress redistribution and the spatial distribution of soft spots[23–26], elements that echo earlier discussions on mechanical responses and rheological properties. By quantifying the spatiotemporal correlations within these rearrangements, we propose a methodological framework capable of predicting collective rearrangements.

RESULTS

The confluent jamming transition is not unique

To investigate the mechanical behavior of dense epithelial tissues under substantial deformation, we employed a Voronoi-based Vertex model[9,21]. The cell centers $\{\boldsymbol{r}_i\}$ and their geometric configurations are derived from Voronoi tessellation. The biomechanical interactions are captured through a dimensionless mechanical energy functional[27] expressed as: $\mathcal{E} = \sum_{i=1}^{N}[\kappa_A(a_i - 1)^2 + (p_i - p_0)^2]$, where a_i and p_i are the dimensionless area and perimeter of each cell, κ_A is the rescaled area elasticity, and p_0 is the *preferred cell shape index* illustrating the cells' homeostatic shape (see "Methods"). To probe the tissue response, we applied quasi-static simple-shear deformation using Lees-Edwards boundary conditions. Strain was incrementally increased, and the FIRE algorithm was used to minimize energy (see "Methods").

In the absence of shear, it has been demonstrated that the preferred cell shape index p_0 drives a rigidity transition at $p_0 = p_0^* \approx 3.81$, where the linear response shear modulus vanishes[20]. Recent studies[9,28] have shown that beyond this transition point, in the liquid phase ($p_0 > p_0^*$), the modeled monolayer can undergo strain-stiffening, indicating a gain in rigidity upon strain application. In our quasi-static shearing protocol, we explore beyond the linear response shear startup regimes and into the large deformation or steady-shear limit. In this regime, the tissue exhibits plastic flow primarily through cell-cell rearrangements, or T1 transitions. Here, the tissue's yield stress is given by

$$\sigma_{yield} = \lim_{\dot{\gamma}\to 0}\langle\sigma(\dot{\gamma})\rangle \tag{1}$$

Where σ is the xy-component of the stress tensor. The average is taken over all strain values in the steady shear regime. As illustrated in Fig. 1a, while the startup shear modulus $G_0 \equiv \lim_{\gamma\to 0}\partial\sigma/\partial\gamma$ (see Methods, Eq. (11) for the calculation of shear modulus) vanishes[9] at the rigidity transition $p_0 \approx 3.81$, signaling a solid-to-fluid transition, the yield stress σ_{yield} does not disappear. Instead, it vanishes at a greater cell shape index, $p_0 \approx 4$. This suggests a marked difference in tissue responses between the transient shear startup and steady-shear regimes.

Under steady shear and at shape indices higher than the rigidity transition associated with shear startup (i.e., at $p_0 > p_0^*$), initially fluid-like systems can intermittently exhibit solid-like behavior before reverting to fluid-like states after yielding (Fig. 1(c)). Here the solid-like states are characterized by a non-zero shear modulus,(e.g., states c, d, e in Fig. 1c), while states that do not resist shear deformation, indicated by having zero shear modulus, are fluid-like (e.g., states a, b, f in Fig. 1(c)). To transition from state b to state c, the system gains rigidity under shear, moving from a fluid-like to a solid-like state. Stress then builds up, as indicated by edges experiencing high tension (Fig. 1e). Once sufficient stress is stored, the system yields, relaxing this stress via collective rearrangements, commonly referred to as avalanches, and transitions from state c to state d.

In the steady-shear regime, we can compute the instantaneous shear modulus (see "Methods") to quantify solid vs. fluid-like states. The solid-fluid coexistence is reflected in the bimodal distribution of the shear modulus $p.d.f(G)$ shown in Fig. 1b, where the fluid phase is associated with a peak near the numerical noise floor of the shear modulus ($\sim 10^{-12}$), while the solid phase corresponds to a finite shear modulus. The shifting behavior of the distributions can be quantified by the fraction of solid states ρ_{solid} shown in Fig. 1b. States below the rigidity transition $p_0 = p_0^* \approx 3.81$ are therefore always in the solid phase, which we term a **pure solid**. In the range $p_0 \in [3.81, 4]$, ρ_{solid} drops below 1, indicating a solid-fluid coexistence, which we refer to as **marginal**. For $p_0 > 4$, the simulated tissue always remains in the fluid phase as it cannot build up stresses in response to shear strain. This is consistent with the yield stress vanishing at $p_0 \simeq 4.0$. The fact that the material response depends on the application of shear is reminiscent of shear jamming in granular materials, where a state below the isotropic (un-sheared) jamming threshold can be jammed with the application of shear[29–32]. The coexistence of solid and fluid phases also has analogs in dense suspensions near shear jamming[33] and discontinuous shear thickening[10,34].

Predicting the tissue yield stress using a refined Soft Glassy Rheology model

Given the continuous behavior of yield stress across the pure solid - marginal state transition, we aimed to develop a unified model to deepen our qualitative understanding of the steady-shear regime properties using the Soft Glassy Rheology (SGR) framework[35,36]. In the SGR model, mesoscopic elements, characterized by an elastic constant k and local strain l, are confined within energy traps E, where they accumulate elastic energy as macroscopic strain increases, approaching a yield point either directly or through an activated "hop" driven by mechanical fluctuations from the yielding of neighboring elements. The material's dynamics under shear are governed by the probability distribution $P(E, l, t)$ evolving in time t, which follows the Fokker-Planck equation[35,36]:

$$\frac{\partial}{\partial t}P(E,l,t) = -\dot{\gamma}\frac{\partial P(E,l,t)}{\partial l} - g_0 e^{[E-kl^2/2]/x}P(E,l,t) + g(t)\rho(E)\delta(l). \tag{2}$$

The first term in Eq. (2) represents the motion of the elements driven by the applied shear rate, $\dot{\gamma}$. The second term describes thermally activated hopping from a trap with an effective depth of $E - kl^2/2$, which corresponds to the remaining distance to yielding. x and g_0 represent the mechanical noise in the system akin to temperature and the hopping rate, respectively. The final term represents the transition to a new trap with energy E drawn from a quenched random distribution $\rho(E)$. The Dirac-delta function $\delta(l)$ reflects the assumption that the local strain l is reset to zero after yielding. The total yielding rate at time t, $g(t)$, is explicitly defined in the SI text (see SI).

In the SGR model, the choice of the functional form of $\rho(E)$ critically influences material behavior[36]. Direct measurement of energy

https://doi.org/10.1038/s41467-025-58526-7

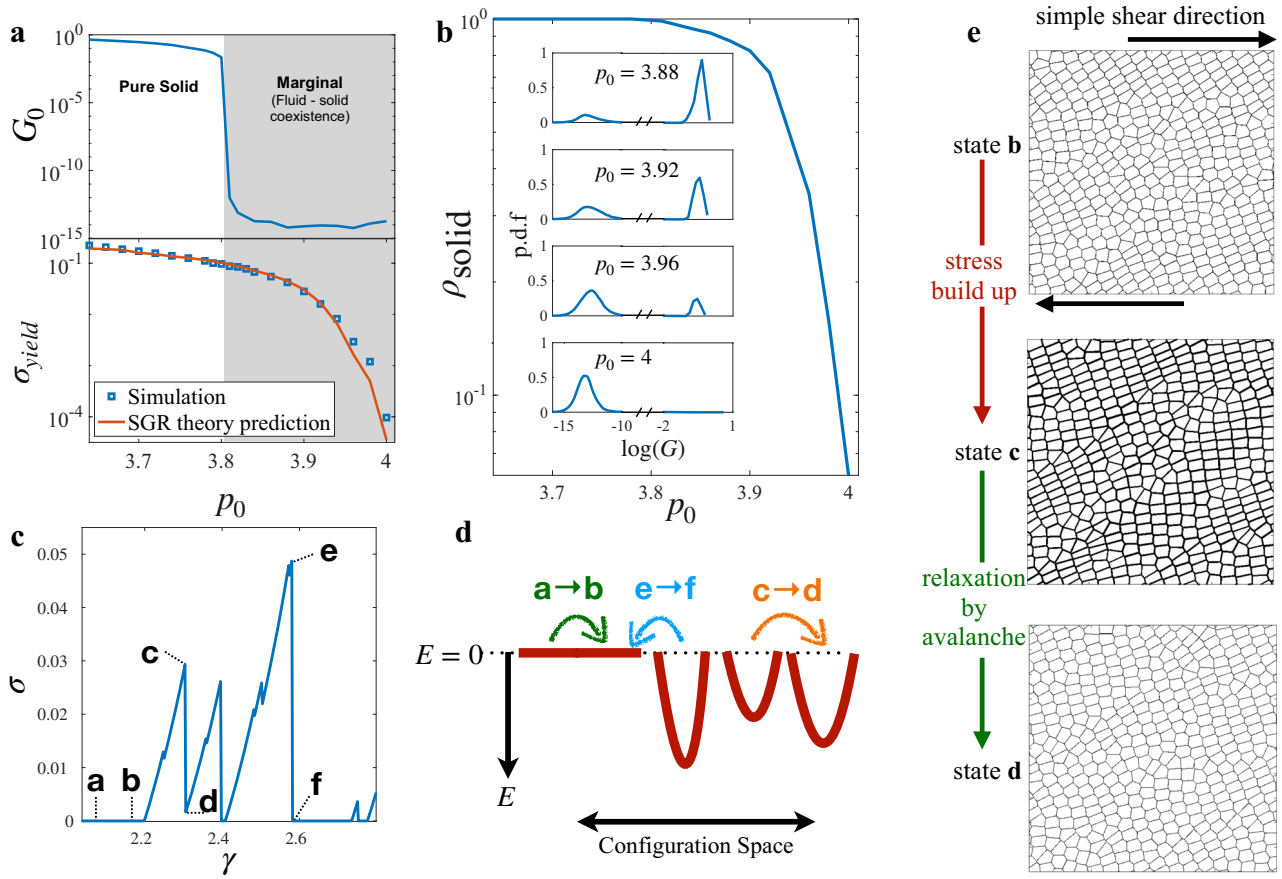

Fig. 1 | Shear Response and Yielding Behavior. a Distinct behaviors in shear startup and the steady-shear regime. Top: The shear modulus of the unsheared tissue ($\gamma = 0$). The shear modulus is obtained using linear-response calculation (see "Methods"). Bottom: The yield stress σ_{yield} obtained from the steady-state shear regime of quasi-static simulations is compared with that obtained from the SGR model, where the only fitting parameter in the model---the elastic constant of an element---was chosen to be $k = 0.0386$. **b** The probability of finding the system in solid state as a function of p_0. Inset: Distribution of tissue stress at different p_0. **c** Stress-strain curve example showing different yielding types: a fluid state yields to another fluid states a → b, a solid state yields to another solid one c → d, and a solid state yields to a fluid state e → f. **d** Schematic of the dynamics of elements in the SGR model: The energy landscape of the material consists of traps with different depths E drawn from a distribution $\rho(E)$ that characterizes the structural disorder of the material. Yielding events are captured by transitions from one trap to another. The three types of transitions illustrate the transitions observed in the simulation. **e** Simulation snapshots at different stages of a stress buildup and relaxation process. The edge thickness represents the edge tension, with thicker edges indicating higher tension. Here, the states correspond to the ones labeled in panel **e**. Source data are provided in a Source Data file.

barrier distributions is challenging, leading prior studies to adopt generic or ad hoc assumptions about $\rho(E)$, such as an exponential distribution[37–40]. In this work, we introduce a novel approach based on the distinct mesoscopic tissue phases observed: (1) fluid elements with zero yielding energy ($E = 0$) and (2) solid elements with finite yielding energy ($E > 0$). Consequently, we propose a refined $\rho(E)$:

$$\rho(E) = f_0\delta(E) + (1 - f_0)\frac{E^{\kappa-1}e^{-E/x_0}}{\Gamma(\kappa)x_0^{\kappa}}. \quad (3)$$

Here, f_0 denotes the probability of an element transitioning to a state with $E = 0$, while $1 - f_0$ corresponds to transitions into states with energy sampled from a k-gamma distribution, parameterized by the mean x_0 and shape factor κ, and $\Gamma(\kappa)$ is the Gamma function. This is based on the previous observation that the energy barriers to the T1 transition follow a k-gamma distribution[20,41] with $\kappa \approx 2$. Together, Eqs. (2) and (3) describe three potential transitions in the energy landscape, as depicted in Fig. 1: (1) fluid–to–fluid a → b, (2) solid–to–solid c → d, and (3) solid–to–fluid e → f.

We next examine the steady state behavior of Eq. (2) in the quasi-static limit ($\dot{\gamma} \to 0$), with details shown in the SI text. This behavior is governed by three parameters: the dimensionless ratio of mechanical noise to mean yielding energy $\chi = x/x_0$, the probability f_0 of transitioning to a fluid state, and the elastic constant k of solid elements.

An important aspect of the SGR model is that the fluctuations driving rearrangements originate from the mechanical noise generated by other surrounding rearrangement events in the system. These fluctuations are analogous to the energy released during yielding events observed in our simulations. To correlate this mechanical noise with our empirical data, we introduce the following relationship:

$$\chi = \frac{x}{x_0} \propto \frac{\langle \Delta E \rangle}{\langle E \rangle}. \quad (4)$$

Here, $\langle \Delta E \rangle$ represents the average energy dissipated during yielding events, while $\langle E \rangle$ denotes the average energy of cells in the solid state. Next, by analyzing the steady-state solution of Eq. (2), we determine the probability that an element is in the solid phase as a function of f_0 (see SI, Eq. S.9). This precisely corresponds to ρ_{solid} in our simulations (Fig. 1b). Finally, we treat the elastic constant k as independent of the shape index p_0. Given that both $\langle \Delta E \rangle / \langle E \rangle$ and ρ_{solid} depend on p_0, the yield stress predicted by the SGR model (see SI) effectively varies only with p_0. This approach contrasts with previous studies that employed the SGR model[37–39,42], in which $\chi = x/x_0$ was often

https://doi.org/10.1038/s41467-025-58526-7

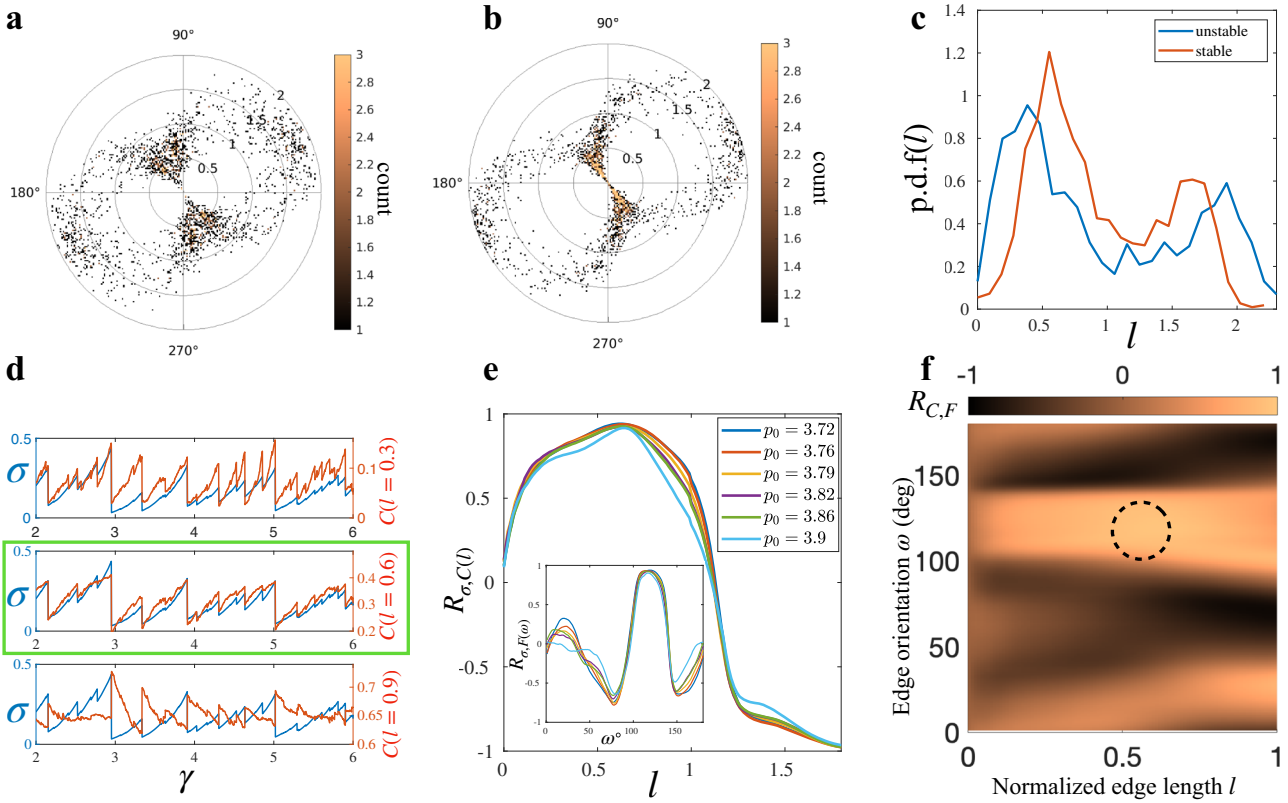

Fig. 2 | A new approach to infer tissue stress. a Polar distribution of cell edge vectors in a stable state. **b** Polar distribution of cell edge vectors in an unstable state. **c** Edge length density distribution at different instability. Panels (**a**–**c**) were generated using $p_0 = 3.72$. **d** The stress-strain curve is overlaid with $C(l)$-strain curve at different l. The green box highlights the trace with a high correlation between σ and $C(l)$. **e** The correlation between tissue stress and the cumulative edge length distribution $R_{\sigma,C(l)}$ suggests a robust critical normalized edge length l^*. Inset: The correlation between tissue stress and the proportion of edges at different orientations $R_{\sigma,F(\omega)}$. **f** Color-plot of the correlation $R_{C,F}$ between edges length distribution and edges orientation distribution. The black-dashed circle indicates the region where the correlation is maximized, from which l^* could be determined. Source data are provided in a Source Data file.

treated as a fitting parameter. In our research, we derive χ directly from simulation data, enhancing the predictive accuracy of our theoretical results and distinguishing our use of the SGR model as predictive rather than merely descriptive. In Fig. 1(a), we plot the SGR-predicted yield stress as a function of p_0, demonstrating that the SGR model accurately predicts the vanishing point of the yield stress and its dependence on the cell shape index $\sigma_{yield}(p_0)$.

The dual-state SGR model identifies two primary mechanisms responsible for the yield stress transition: **(1)** As p_0 increases, states with zero yielding energy barriers become more prevalent, leading to frequent yielding under deformation. This behavior is depicted by transitions such as a → b and e → f in Fig. 1d; **(2)** Concurrently, mechanical noise from stress redistributions approaches the scale of the yielding energy barriers, enhancing the likelihood of solid-solid transitions through activated processes induced by neighboring rearrangements, as illustrated by c → d and e → f.

A new method to infer tissue stresses based on instantaneous snapshots

The coexistence of phases observed in the Vertex-based model reinforces the idea that tissues behave as yield stress materials while also exhibit fluid-like behavior. When combined with Soft Glassy Rheology (SGR) theory, this coexistence allows for predictions for tissue yield stress based on the homeostatic cell shape index p_0. Given p_0, the Vertex based model could also provide an estimate of the instantaneous tissue stress using Eqn. (10). However, determining the homeostatic target shape index p_0 remains an experimental challenge. In contrast, segmented cell configurations in tissues are experimentally accessible and have been utilized in several non-invasive stress inference methods such as Bayesian Inference method[43,44] and the image-based Variational method[45]. Although the Bayesian Stress Inference method proposed by Ishihara and Sugimura[44] has been applied to various systems, including Drosophila notum, retinal ommatidia, germband, and the quail early embryo[46,47], its results strongly depend on a prior distribution of edge tension and cell pressure, which is not necessarily normally distributed as originally proposed. Additionally, the method faces the challenge of having more unknown variables than constraints. In contrast, the Variational Method proposed by Noll et al.[45] addresses the issue of under-constrained variables but relies on a computationally expensive fitting approach. Here, we propose a fast, non-invasive, image-based tissue stress inference method that is both convenient and accurate. It has been shown that edge length distribution is closely related to the distance to yield stress in monolayers[19]. However, the connection between edge length distribution and tissue stress has not been quantified. In this work, we demonstrate that the cumulative distribution of edge length elegantly serves as a robust estimator of tissue stress.

In systems under deformation, the configuration exhibits anisotropy, with preferred orientations dictated by the deformation direction. To analyze this anisotropy and its evolution with strain, we examined the distribution of edge vectors in the system, represented as polar distributions. In these distributions, color encodes the frequency of edges with lengths and orientations defined by radial distance and azimuthal angle, respectively. The polar distribution for an isotropic system therefore looks like a circle with dots scattered randomly inside. This was not observed in our system due to the anisotropy. To systematically study across different systems and time frames, we used the normalized edge length $l = L/\bar{L}$, obtained by normalizing the edge lengths by the average edge length in the

https://doi.org/10.1038/s41467-025-58526-7

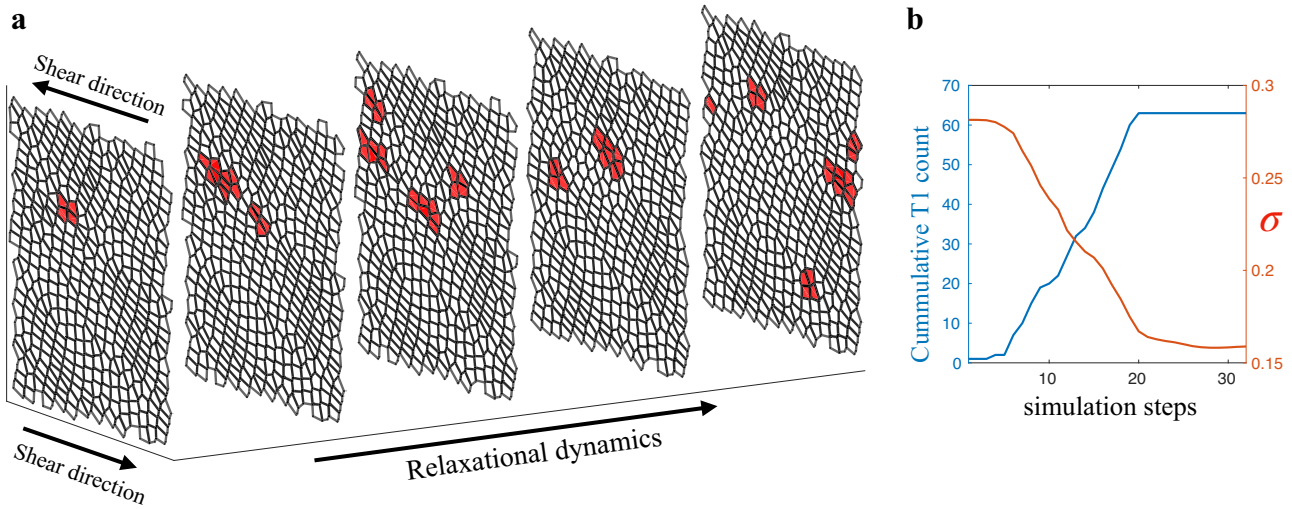

Fig. 3 | Spatiotemporal map of plastic events. a Space-time map of plastics rearrangement in the form of T1 transition during an avalanche. Cells that participated in T1 transitions are labeled in red. The example avalanche was selected from a system at $p_0 = 3.72$. **b** Number of accumulative plastic rearrangement and tissue shear stress as the avalanche progresses.

current snapshot. Fig. 2a displays the polar distribution of the normalized edge vectors $\vec{l}$ in a low-stress, stable system far from yielding. Conversely, Fig. 2b depicts the edge vector distribution in a high-stress, unstable system close to yielding. In both cases, anisotropy emerges, with longer edges aligning with the shear direction (about 45 degrees with respect to horizontal) and shorter edges perpendicular to it. However, the trend is more pronounced in unstable systems, illustrated by the red color band representing high population of short edges with orientation about 135 degrees with respect to horizontal (Fig. 2b), implying a connection between instability and edge vector distribution. Furthermore, these polar plots reveal a strong correlation between edge length and orientation in deformed configurations.

The correlation between edge length and orientation suggests that the edge length distribution can effectively represent the overall edge vector distribution. To investigate how edge configuration influences instability, we compared the edge length distributions of stable and unstable states. As illustrated in Fig. 2c, both distributions exhibit a bimodal shape due to anisotropy. However, in the distribution of the unstable system, the separation between the two peaks is larger, reflecting stronger anisotropic effects and an abundance of short edges, which are more prevalent in the unstable configuration. This motivated us to study the evolution of the edge length distribution as strain increases.

By investigating the evolution of the edge length cumulative distribution $C(l)$ in our quasi-static simple shear simulations, we observed a correlation between $C(l)$ and σ, with the correlation level depending on l. As shown in Fig. 2d, while the correlation $R_{\sigma,C}$ between tissue stress σ and $C(l)$ varies with l, there exists a range of l where $C(l)$ is highly correlated with σ. We denote the l value that maximizes the correlation $R_{\sigma,C}$ as l^*, and the corresponding cumulative distribution $C(l^*)$ as C^* (also see SI text and SI Fig. S1 for details). Interestingly, both l^* and $R_{\sigma,C}$ remain robust with changes in p_0, with the critical correlation R_{σ,C^*} exceeding 0.9, as shown in Fig. 2e. Given the strong correlation between C^* and σ, as well as the fact that cell edge lengths can be directly extracted from imaging, C^* could serve as a non-invasive metric for inferring tissue-level stress.

While $l^* \approx 0.61$ is consistent across various p_0 values in our quasi-static simulations, its practical value may depend on system properties and the shearing direction. Thus, developing a metric to experimentally determine l^* is crucial for the stress inference method. Recognizing the strong relationship between edge length and orientation in anisotropic systems, we investigated tissue stress and edge orientation correlations. To quantify the edge orientation distribution, we used the proportion of edges a given orientation ω:

$$F(\omega) = \frac{N(\omega - \Delta\omega, \omega + \Delta\omega)}{N_{\text{edges}}} \tag{5}$$

Here, $N(\omega - \Delta\omega, \omega + \Delta\omega)$ represent the number of edges in a cone with the open angle of $2\Delta\omega$ at the ω direction and N_{edges} is the total number of edges in the system. In this section, all angular values are in degrees. Tracking the evolution of $F(\omega)$ at different ω as strain increased, we observed a critical orientation $\omega^* \approx 120°$, where $F(\omega)$ was highly correlated with tissue stress, with a correlation coefficient $R_{\sigma,F(\omega^*)}>0.9$ (Fig. 2e inset). Although $R_{\sigma,F}$ depends on the cone wideness $\Delta\omega$, which we chose as $\Delta\omega = 18° = \pi/10$ to optimize $R_{\sigma,F}$, the critical orientation ω^* is independent of $\Delta\omega$. Additionally, ω^* was robust across variations in p_0 (Fig. 2e inset). Given the high correlations $R_{\sigma,C}$ and $R_{\sigma,F}$, the critical edge length l^* could potentially be determined from the correlation between edge length and edge orientation, $R_{C,F}$. As suggested by Fig. 2e, we only focus on the range $l < 1$ in which $C(l)$ is known to positively correlates with tissue stress σ. By computing the correlation $R_{C(l),F(\omega)}$ at different (l, ω), we identified a region where the correlation is exceptionally high (greater than 0.93), as indicated by the dashed circle in Fig. 2f. The l values in this region align well with the critical edge length l^*, suggesting that l^* can be estimated as the normalized edge length value l maximizing $R_{C(l),F(\omega)}$. With l^* in hand, ones could used $C^* = C(l^*)$ to extract an estimation of the tissue stress as it evolves during the deformation process. Our stress inference method could be conveniently validated by experiments such as the monolayer stretching protocol[3]. Although C^* could be used directly as the inference for tissue stress, various functional relationships can be established between C^* and stress (see SI text).

Dynamics of tissue plasticity

So far, we know that for a system in the coexistence phase to transition from solid to fluid, a collective rearrangement event is required to significantly remodel the configuration. However, the mechanism that governs the occurrences of these events and the evolution of the system during the events is still not fully understood. To explore the yielding behavior of biological tissues, it is essential to describe the dynamics of plastic events during avalanches. In this study, we examine the plasticity dynamics by investigating the spatiotemporal

https://doi.org/10.1038/s41467-025-58526-7

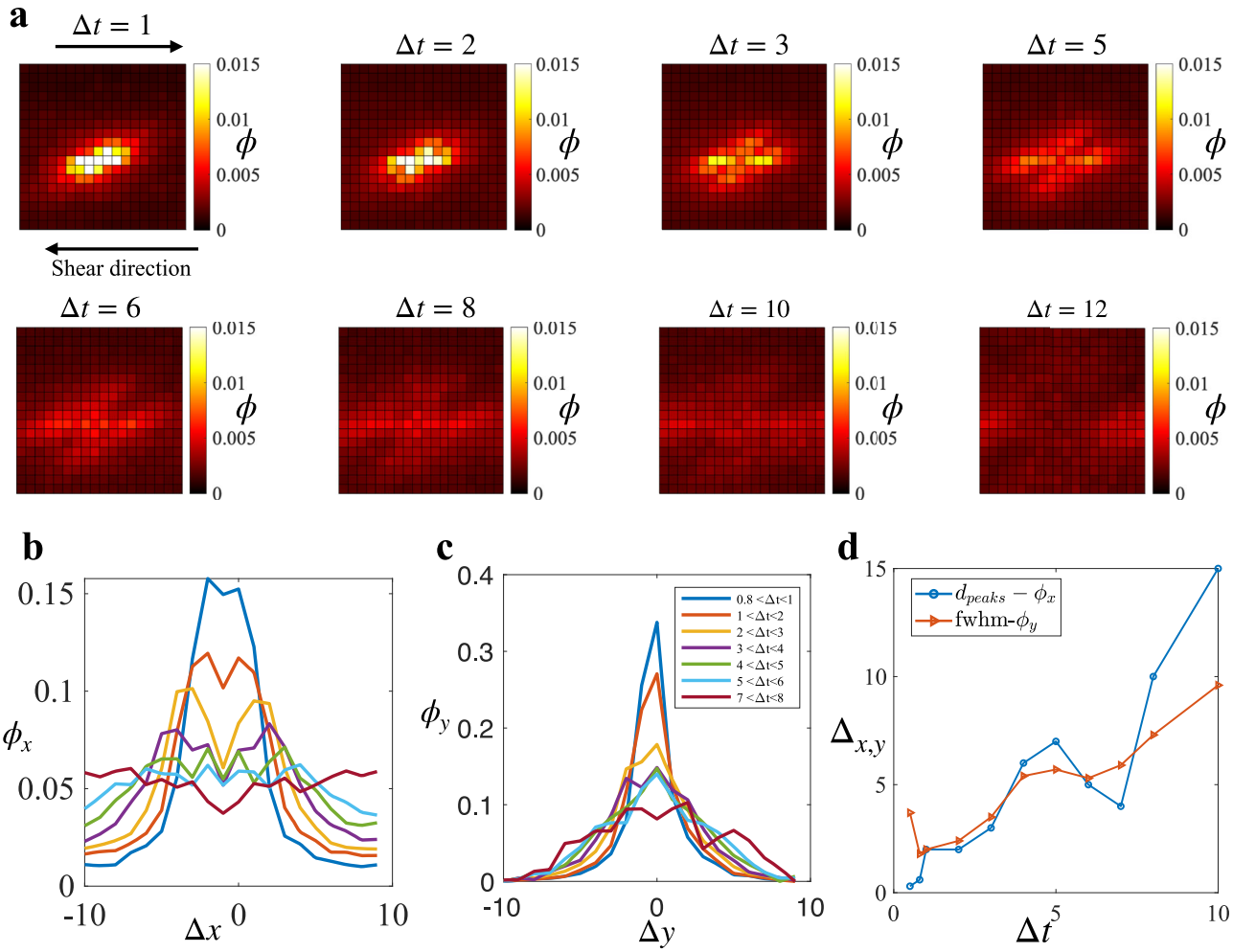

Fig. 4 | Propagation of plastic events. a Evolution of the probability field ϕ at $p_0 = 3.72$. Each image corresponds to the probability field at a particular time lag Δt. Bright regions indicate a high probability of finding another rearrangement in the region relative to the causal rearrangement. **b** Spatial distribution of the correlation field ϕ_x as a function of the relative horizontal position Δx. The distribution has a diffusing bimodal shape, indicating a convection process alongside diffusion. **c** Spatial distribution of the correlation field ϕ_y as a function of the relative vertical position Δy. The distribution is bell-shaped, with the width of the bell increasing as time progresses, indicating a pure diffusion process. **d** The separation of the peaks in ϕ_x and the Full Width at Half Maximum (FWHM) of ϕ_y as functions of the time lag Δt. Source data are provided in a Source Data file.

evolution of the plastic rearrangements created by other rearrangements during an avalanche[48,49]. Fig. 3a displays a space-time plot of the occurrences of T1 transitions during an avalanche, with the cells labeled in red indicating participation in the T1 transitions.

As depicted in Fig. 3a, an avalanche involving numerous plastic rearrangements can originate from a single T1 transition, which we refer to as the initial trigger. Starting from the initial trigger, the stress redistribution from each event can also stimulate surrounding cells to become unstable and undergo T1 transitions. These soft cells, whose mechanical characteristics are distinct from the surrounding cells, experience larger deformation than the neighboring cells and have been observed in multicellular tumor spheroids using 3D light microscopy[50]. From an amorphous solid point of view, these cells are referred to as soft spots[23–26] or Shear Transformation Zones[51,52]. This cascade of cellular rearrangements can therefore lead to an avalanche, which continues until the population of soft spots is sufficiently depleted. In Fig. 3b, we show the number of accumulated T1 transitions and the tissue shear stress during a typical avalanche. The stress relaxation due to an avalanche is therefore the origin of the discontinuous yielding of stress during quasistatic shear. In Fig. 3a, the location of rearrangements over time suggests a preferred direction for avalanche propagation. In order to quantify this and establish a causal relationship in time, we define a two-point, two-time correlation function:

$$\phi(\mathbf{r}, \Delta t) = \langle P(\mathbf{r}_0, t_0) P(\mathbf{r}_0 + \mathbf{r}, t_0 + \Delta t) \rangle, \quad (6)$$

where $P(\mathbf{r}, t)$ is a binary field, representing the occurrence of a T1 transition (1 if a T1 transition occurs at $\mathbf{r}$ and time t, and 0 otherwise). $\langle \ldots \rangle$ denotes spatial and ensemble averaging. With this definition, ϕ represents the conditional probability of observing a T1 transition at location $\mathbf{r}_0 + \mathbf{r}$ and time $t_0 + \Delta t$, given that a transition has already occurred at $(\mathbf{r}_0, t_0)$.

In Fig. 4a, we illustrate the evolution of the field ϕ as Δt increases. The field ϕ resembles a wave that propagates away from the causal rearrangement and is primarily in the x-direction, aligned with the direction of the external shear force. The evolution of the field ϕ reflects the interplay between the stress redistribution from a plastic rearrangement and the population of soft spots which could rearrange under the effect of the strain field.

We first focus on the angular dependence of ϕ, which shows an anisotropic four-fold pattern. This anisotropy is consistent with the stress redistribution field due to a rearrangement in an elastic medium as predicted by elastoplastic models[19,53]. However, it differs from the

https://doi.org/10.1038/s41467-025-58526-7

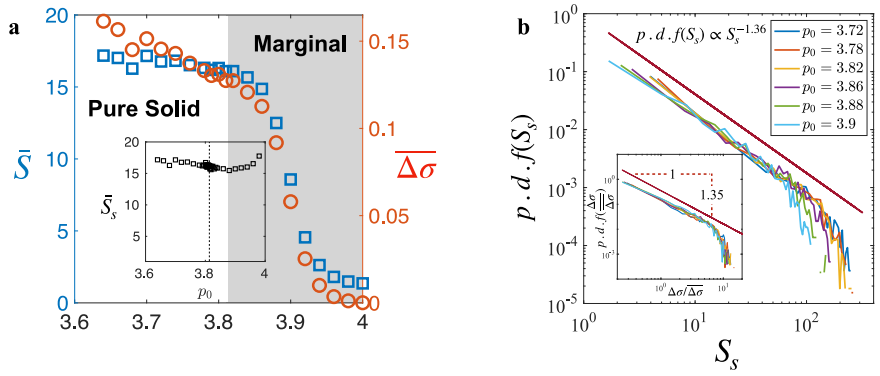

Fig. 5 | Avalanches statistics. a Dependence of average yielding size $\bar{S}$ and average stress relaxed $\overline{\Delta\sigma}$ on p_0. Inset: Dependence of average avalanches size $\bar{S}_s$ on p_0. **b** Distribution of avalanche size follows a power-law distribution. Inset: Distribution of scaled average stress relaxed by avalanches also follows the same power law. Source data are provided in a Source Data file.

isotropic probability field observed in ductile, soft disk systems[54]. This contradiction likely arises from the difference in shape anisotropy between soft disks and cells in our system. While soft disk systems exhibit minimal particle shape anisotropy, cells in our system can sustain large deformations and have highly anisotropic shapes. Consequently, deviatoric strain triggers rearrangements in soft disk systems, whereas simple shear strain is responsible for triggering rearrangements in our system.

To better understand how the rearrangement probability field propagates, we looked at $\phi_x = \frac{\phi(x,y=0)}{\sum_x \phi(x,y=0)}$ and $\phi_y = \frac{\phi(x=0,y)}{\sum_y \phi(x=0,y)}$ separately. ϕ_x, as observed in Fig. 4b, is a bimodal distribution that evolves in time such that the distance between the two peaks d_{peaks} increases as time progresses. The diffusing bimodal distribution suggests that the propagation results from a combination of convection and diffusion, and the drift velocity could be captured by the rate at which the peaks' separation increases. Conversely, ϕ_y is a bell-like shape distribution that gets broaden over time (Fig. 4c), indicating that the propagation in the y-direction is similar to a purely diffusion process with the diffusivity can be captured by the evolution of the FWHM. Fig. 4d shows that d_{peaks} increases faster than the FWHM-ϕ_y. Since the rearrangement probability field is the result of the shear stress redistribution and the population of soft spots, the propagating mechanism of the field also should agree with the propagation of the stress redistribution.

The tendency of shear stress redistribution to propagate in the direction of shear has also been observed in particle-based systems governed by inverse-power-law pairwise potentials[49]. This behavior bears a resemblance to the propagation of elastic waves. In the theory of elasticity, longitudinal waves, characterized by displacement in the direction of propagation, outpace transverse waves[55]. Moreover, longitudinal elastic waves involve changes in local density[55], akin to the x-propagating excitation wave's modulation of local density via T1 transitions. Conversely, transverse elastic waves do not induce density changes, resembling the infrequent involvement of T1 transitions in y-propagating excitation waves. Notably, the mechanism driving stress redistribution to preferentially propagate in the shear direction appears universal, independent of p_0. However, since p_0 governs the elastic response in our system, with higher values corresponding to a less elastic state, there is a negative correlation between the stress redistribution wave's speed and p_0.

Statistics of tissue avalanches

In addition to the universal propagation mechanism, we wondered if the statistics of tissue yielding events also exhibit universality. In Fig. 5a, both the average yielding size $\bar{S}$, denoting the total number of T1 transitions after a yielding event, and the average stress drop, representing the amount of stress relaxed by the event, exhibit the same dependence on p_0. In the solid regime, while the stress decreases with increasing p_0, the average yielding size shows minimal variation. This trend of $\bar{S}$ versus p_0 is akin to that observed in Fig. 1b for the proportion of the solid state.

However, in the marginal phase, there are different types of yielding events as discussed previously (Fig. 1c). In the yielding events that occur while the system is fluid-like, illustrated by the a → b transition in Fig. 1c (Type I), the tissue lacks rigidity and therefore is unable to transmit stress to initiate a cascade of rearrangements. Conversely, yielding events following a solid state, illustrated by c → d and e → f transitions in Fig. 1c (Type II), tend to be cascading as the rigid tissue is capable of propagating the stress redistribution. It is this latter type that we refer to as tissue avalanches from now on. Since the avalanches growing mechanism is universal, we expect their statistics to be independent of p_0 as well.

Excluding yielding events of type I from the analysis and specifically analyzing only the avalanches, we indeed find that the average avalanche size $\overline{S_s}$ does not vary significantly with p_0 (Fig. 5a inset), suggesting universal avalanches size statistics. To rigorously assess this universality, we examine the distribution of avalanche sizes across various p_0 values (see Fig. 5b). We observe a consistent power-law distribution, reminiscent of the Gutenberg-Richter law observed in earthquakes[56,57], with an exponent $\tau = -1.36$, which agrees with the analogous exponent observed in overdamped elastoplastic models under shear[58,59] and in vertex model on spherical surface[60]. This shared characteristic suggests a parallel between biological and seismic avalanches and supports the argument that the vertex model and epithelial tissues belong to the universality class of plastic amorphous systems.

Furthermore, we find that the same power law applies to the distribution of average stress drops during avalanches when scaled by the average (Fig. 5b inset). This collapse after rescaling implies that the stress relaxation mechanism via avalanches is independent of the shape index p_0, and p_0 only affects the average stress relaxed by governing tissue overall stiffness. Moreover, the similarity in the stress drop distribution and avalanches size distribution indicates that each plastic rearrangement, on average, releases a similar amount of stress that depends only on p_0. The convergence of these distributions suggests that the growth of avalanches remains unaffected by changes in p_0, providing additional evidence for the universal propagation mechanism discussed earlier.

Predicting tissue avalanches based on static structural information

While the first cells to undergo a T1 transition trigger the avalanche, in order for the avalanche to grow, it is necessary to have soft spots in the system that are susceptible to undergo T1s. In the framework of the

https://doi.org/10.1038/s41467-025-58526-7

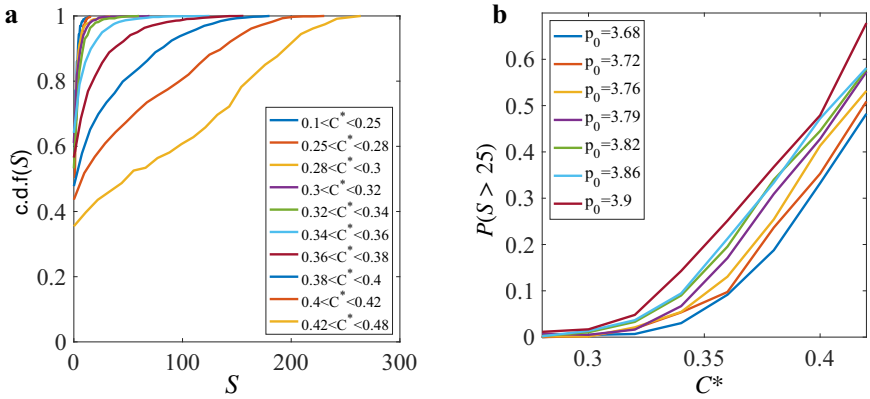

Fig. 6 | Predicting avalanches. a c.d.f(S) at different C^* level at $p_0 = 3.79$. **b** Probability of having avalanches of size greater than 25 at different C^*. Source data are provided in a Source Data file.

elastoplastic model, it has been established that the distance to yield x, which represents the additional stress required to trigger a yielding event, follows a power-law distribution, $p(x) \propto x^{\theta}$ [61–63]. The exponent θ has been suggested as a measure of the system's instability, with a higher value indicating a more stable state.

In the vertex-based model family, it has been proposed that the distance to yield x exhibits a linear relationship with the length of cell edges L, and that the distribution of edge lengths should follow the same power-law behavior as $\rho(x)$[19]. While this argument establishes a connection between system configuration and instability, the efficacy of using the distribution of short edges to describe instability remains uncertain.

To address this ambiguity, we investigate this concept within our Voronoi model and observed an intriguing correlation between the exponent θ and system instability (see SI text and SI Fig. S2). However, θ is not a reliable metric because it is derived from a power-law fit that heavily depends on the range of fitting[19]. In practice, the cumulative distribution function (c.d.f) of L exhibits power-law behavior only within a specific range, which varies from sample to sample. Therefore, we propose using C^* as the parameter of instability to avoid the uncertainties and biases associated with fitting.

Using C^* as the parameter of instability, with higher C^* corresponding to a more unstable state, we observed a relationship between instability and avalanche size. To quantify the relation between instability and avalanche size, we focus on the failure states, i.e states that are about to yield, indicated by having a stress drop in the next strain step and a corresponding avalanche. We computed C^* for those states and then grouped the avalanche sizes based on C^* (Fig. 6a). At low C^*, if the tissue yields, the size of the yielding event is likely to be small, indicated by a rapid increase to 1 in the cumulative distribution function (c.d.f.) of S. As C^* increases, the likelihood of larger yield events grows. The probability of observing an avalanche of size 25 or greater is summarized in Fig. 6b.

While C^* can provide predictions about avalanche size, it cannot determine when an avalanche will occur. Therefore, we require an additional tool to forecast yielding events. In amorphous solids, the locations of plastic rearrangements during an avalanche largely depend on the material's structural configuration, with areas more likely to experience plastic events called soft spots. Various frameworks have been proposed to link structure and plasticity, such as the Shear Transformation Zone theory[25,51,52,64,65] and lattice-based models. The most promising theoretical approach for predicting the locations of soft spots involves identifying these areas based on soft vibrational modes[24,66–68]. As a system approaches a plastic rearrangement, at least one normal mode is supposed to approach zero frequency[24,69,70]. However, the vibrational mode analysis is not applicable to the vertex-based model family due to the cuspiness of the energy landscape[20,41]. In such systems, the energy cusp at a plastic event prevents the corresponding low-frequency mode from vanishing as it would in systems with smooth, analytic energy landscape. As shown in the SI Fig. S3, in our system, no low-frequency mode approaches zero frequency except at the onset of the plastic event. Hence, an alternative approach is necessary.

In our model, the deformation of edges immediately following shear strain is deterministic. Through simple geometry, we deduce the existence of a range of orientations wherein edges are prone to shortening upon shearing, rendering them more susceptible. In the vertex model, under the condition $\dot{\gamma} \ll 1$, the change in edge length δL due to shear is approximated as $\delta L \approx \dot{\gamma} L \sin(2\phi)$, where L and ϕ represent the edge length and orientation, respectively. Consequently, in the vertex model, the most susceptible orientation is $\frac{3\pi}{4}$. If an edge is sufficiently weak (or short) and happens to align with this susceptible orientation, it may yield under the influence of shearing, potentially triggering further rearrangements in its vicinity. We refer to these susceptible edges as triggers. Since triggers are local elements, their presence is not captured by the cumulative distribution function of edge lengths, c.d.f(L), thereby explaining why C^* alone cannot predict imminent system failure. In summary, the presence of a trigger is the necessary condition, while a high C^* in the current state is the sufficient condition for a large avalanche in a tissue monolayer.

Discussion

We studied the response of simulated tissue monolayers to external quasi-static shear stress in the long-term steady-shear regime. Our work suggests that for a model tissue monolayer initially in a fluid state, it behaves like a yield-stress material in the shear buildup regime but eventually enters a marginal phase in the long-term steady shear regime. Incorporating the coexistence phase into to the SGR model, we elucidated the discrepancy between the rigidity transition and the yield stress transition observed in the Vertex model under simple shear.

Besides studying yield stress in the model tissue, we also investigate plasticity, reflected in avalanches of plastic rearrangements. Understanding those local rearrangements would help reveal the mechanism of mechanical homeostasis and reparation in biological tissue. By studying the dynamics of tissue avalanches, we observed a universal propagation mechanism of plastic events that is independent of the shape index p_0 and has two preferred directions, with the direction of the external shear being the one with faster propagation. The rearrangement probability ϕ studied here is closely related to, but not identical with, the stress redistribution predicted by elastoplastic models[19,53] or the strain field due to rearrangement[54]. Instead, ϕ captured the interplay between stress redistribution and spatial distribution of weak spots. Since most edges that participated in T1 transition in our system orient at $-\pi/4$ with respect to the horizontal (see SI, Fig. S4), the positive shear stress is expected to symmetrically

redistribute along the horizontal and vertical directions[19]. Although ϕ does propagate mainly in the horizontal and vertical directions, it does not possess the vertical-horizontal symmetry seen in stress redistribution or in the strain field. This difference arises from the high heterogeneity and anisotropy in the spatial distribution of weak spots. The rearrangement dynamics studied in this work could help identify regions where rearrangements are anticipated in the near future. Predictions based on our analysis are most reliable in systems where external forces dominate cellular activity or under quasi-static conditions. In these scenarios, rearrangements occur systematically, driven solely by stress redistribution from regions of high stress to relax global stress. Conversely, in systems with high cellular activity, rearrangements happen randomly due to the stochastic motion of cells, blurring the impact of stress redistribution. Although capturing avalanches experimentally is challenging due to the competition between various timescales in active tissue, tracking the spatiotemporal evolution of local rearrangements is feasible within timescales where activities such as cell division are negligible. Such experiments could provide valuable evidence to support our analysis of rearrangement dynamics. One such experiment is the fracturing of Trichoplax Adhaerens, during which regions with significant non-affine motion exhibit spatial correlations along the direction of the driving shear force[18].

The universality of tissue avalanches is not only reflected in the propagation of plastic events but also captured by a power-law distribution of avalanche sizes, with an exponent $\tau = -1.36$, strengthening the argument that epithelial tissues behave like plastic amorphous materials. We also propose a metric to not only predict tissue avalanches but also infer tissue stress in highly anisotropic systems based on an instantaneous static snapshot. In finite size system, the cut off avalanches size S_c depends on the system size N as $S_c \propto N^{d_f/d}$, where d_f is fractal dimension of avalanches and d is the dimension of the system[62]. Future possible work can be performed with different system size to obtain the avalanches fractal dimension d_f and further understand the finite size effect on avalanches.

We also propose a metric to not only infer tissue stress based on an instantaneous static snapshot but also predict tissue avalanches. Quantification of tissue-level force and stress is necessary to understand the physics of many biological processes. However, direct measurement of stress in vivo is considerably challenging[71–73]. Compared to other non-invasive methods to estimate tissue stress such as Bayesian Force Inference[44] and Variational Method for Image-Based Inference[45], our approach using C^* offers a simple and fast method to estimate tissue stress. The advantage of C^* lies in its independence from fitting parameters and system properties. Given a segmented movie of a monolayer undergoing deformation, C^* can be easily derived from the segmented images and offers a decent estimate of tissue relative stress evolution during the process without requiring prior knowledge of the monolayer's mechanical properties. The downside of our approach is that it cannot provide a spatial distribution of local stress. The strong agreement between σ_{xy} and C^* is noteworthy, especially since C^* does not incorporate information about edge orientation, which directly affects stress. In an isotropic system, edge length alone is insufficient to infer stress. However, in a system undergoing large deformation and thus highly anisotropic, the influence of edge orientation diminishes, making edge length alone sufficient for stress inference. The impact of shape anisotropy is evident during the buildup phase or when the system is in a fluid state. In these scenarios, edges may have negligible tension, making edge tension independent of edge length. Consequently, it is possible that systems with similar C^* values could exhibit significantly different stress levels.

The impact of triggers on avalanches goes beyond simply initiating them; we observed a significant dependence of avalanche size on the trigger location. By manually shrinking vanishing edges at various locations within the same configuration, we noted that the size of the resulting avalanches varied markedly. This indicates that the location of the initial excitation has a profound influence on the final size of the avalanche. A promising future research direction could involve developing a theoretical framework that moves beyond the mean field approach to more accurately capture the spatial heterogeneity in the tissue.

Methods

Simulation Model

To numerically study the behavior of dense epithelial tissues under large deformation, we use a Voronoi-based version[21] of the Vertex Model[74], where the degrees of freedom are the set of cell centers denoted as $\{\boldsymbol{r}_i\}$ and the geometric configurations of cells are derived from their respective Voronoi tessellation. The biomechanics governing interactions both within and between cells can be effectively represented at a coarse-grained level[27,75], expressed in terms of a mechanical energy functional associated with cell shapes, given by:

$$E = \sum_{i=1}^{N} \left[K_A (A_i - A_0)^2 + K_P (P_i - P_0)^2 \right], \tag{7}$$

where A_i and P_i represent the area and perimeter of the i-th cell, respectively. The parameters K_A and K_P denote the area and perimeter moduli, respectively. The values A_0 and P_0 correspond to the preferred area and perimeter values, with A_0 specifically set to the average area per cell $\bar{A}$. Without the loss of generality, we choose $K_P A_0$ as the energy unit and $\sqrt{A_0}$ as the length unit. This leads to the dimensionless form of the energy

$$\varepsilon = \sum_{i=1}^{N} \kappa_A (a_i - 1)^2 + (p_i - p_0)^2, \tag{8}$$

where $\kappa_A = K_A A_0 / K_P$ represents the rescaled area elasticity, governing the cell area stiffness relative to the perimeter stiffness, $a_i = A_i/A_0$ and $p_i = P_i/\sqrt{A_0}$ are the rescaled area and perimeter, respectively, and $p_0 = P_0/\sqrt{A_0}$ the cell shape index. In this particular work, we studied only the regime with $K_A = 0$ and $K_P = 1$. To investigate the mechanical response of the tissue, we apply simple-shear deformation to the simulated tissues utilizing Lees-Edwards boundary conditions[76]. Initially, strain-free configurations ($\gamma = 0$) are generated with randomly distributed cell centers. The FIRE algorithm[77] is subsequently employed to minimize the energy functional in accordance with Eq. (8). Strain is then incrementally applied in steps of $\Delta\gamma = 2 \times 10^{-3}$ until reaching a maximum value of $\gamma_{max} = 6$. Alongside the modification of periodic boundary conditions to account for the strain, an affine displacement field $\Delta \mathbf{r_i} = \Delta\gamma\, y_i\, \hat{x}$ is applied to the cell centers. Following each increment of strain, the FIRE algorithm is again utilized to minimize the energy functional (Eq.(8)) until the residual forces acting on cell centers fall below 10^{-14}, so that all resultant tissue states are meta-stable. This procedural approach effectively corresponds to investigating the system within the athermal quasi-static limit ($\dot{\gamma} \to 0$). The tissues under examination consist of cell populations with $N = 400$, accompanied by varying cell shape indices p_0. A total of 84 random initial samples were simulated for each set of parameter values. The shape indices were incrementally varied from 3.66 to 4, with a step size of 0.2, except near the rigidity transition $p_0^* = 3.81$. For $3.8 \le p_0 \le 3.82$, the parameter was incremented with a finer step size of 0.02 to study the transition. We calculate the tension, denoted as $\mathbf{T}_{ij}$, acting along an edge $\mathbf{l}_{ij}$ shared by cells i and j using the equation[43,44,78]

$$\mathbf{T}_{ij} = \frac{\partial \varepsilon}{\partial \mathbf{l}_{ij}} = 2[(p_i - p_0) + (p_j - p_0)]\hat{\mathbf{l}}_{ij}, \tag{9}$$

where $\hat{\mathbf{l}}_{ij}$ represents the unit vector along $\mathbf{l}_{ij}$. Furthermore, the global tissue shear stress σ can be obtained by

$$\sigma = \sigma_{xy} \equiv \frac{1}{N}\sum_{i<j} T_{ij}^{x}\, l_{ij}^{y}, \tag{10}$$

where T_{ij}^{x} denotes the x-component of $\mathbf{T}_{ij}$ and l_{ij}^{y} stands for the y-component of $\mathbf{l}_{ij}$.

Computing tissue level mechanical linear response

The tissue level mechanical response was quantified by the shear modulus G. We computed G using Born-Huang formulation in the limit of infinitesimal affine strain γ[79,80]:

$$G = \frac{1}{A_{total}}\left(\frac{\partial^2 E}{\partial \gamma^2} - \Xi_{i\alpha} H^{-1}_{i\alpha j\beta} \Xi_{j\beta}\right), \tag{11}$$

where the Roman indexes i, j label cells and Greek indexes α, β denote Cartesian components. $\Xi_{i\alpha}$ is the derivative of the force on cell ith with respect to the strain γ:

$$\Xi_{i\alpha} = \frac{\partial^2 E}{\partial r_{i\alpha} \partial \gamma} \tag{12}$$

H is the Hessian matrix given by the second derivative of the tissue energy E with respect to position cells position:

$$H_{i\alpha j\beta} = \frac{\partial^2 E}{\partial r_{i\alpha} \partial r_{j\beta}} \tag{13}$$

Statistics and reproducibility

The data shown in this work corresponds to the ensemble average over 84 simulations for each p_0 value, unless indicated otherwise.

Reporting summary

Further information on research design is available in the Nature Portfolio Reporting Summary linked to this article.

Data availability

Source data are provided with this paper for the analyzed data. The raw data that support the findings of this study can be independently reproduce using the code made publicly available on GitHub (See Code Availability). Source data are provided with this paper.

Code availability

The custom code developed for this study is available at GitHub Repository (https://github.com/jxhuangphys/sheared_voronoi_model) under the MIT license and in Zenodo repository https://doi.org/10.5281/zenodo.14907889 (https://doi.org/10.5281/zenodo.14907888)[81]. For further inquiries, please contact the corresponding author.

References

1. Bonfanti, A., Duque, J., Kabla, A. & Charras, G. Fracture in living tissues. *Trends Cell Biol.* **32**, 537–551 (2022).
2. Harris, A. R. et al. Characterizing the mechanics of cultured cell monolayers. *Proc. Natl Acad. Sci.* **109**, 16449–16454 (2012).
3. Harris, A. R. et al. Generating suspended cell monolayers for mechanobiological studies. *Nat. Protoc.* **8**, 2516–2530 (2013).
4. Sadeghipour, E., Garcia, M. A., Nelson, W. J. & Pruitt, B. L. Shear-induced damped oscillations in an epithelium depend on actomyosin contraction and e-cadherin cell adhesion. *eLife* **7**, e39640 (2018).
5. Bashirzadeh, Y., Dumbali, S., Qian, S. & Maruthamuthu, V. Mechanical response of an epithelial island subject to uniaxial stretch on a hybrid silicone substrate. *Cell. Mol. Bioeng.* **12**, 33–40 (2018).
6. Cai, G. et al. Compressive stress drives adhesion-dependent unjamming transitions in breast cancer cell migration. *Frontiers in Cell and Developmental Biology* **10**, 933042 (2022).
7. Villemot, F. & Durand, M. Quasistatic rheology of soft cellular systems using the cellular Potts model. *Phys. Rev. E* **104**, 055303 (2021).
8. Merzouki, A., Malaspinas, O. & Chopard, B. The mechanical properties of a cell-based numerical model of epithelium. *Soft Matter* **12**, 4745–4754 (2016).
9. Huang, J., Cochran, J. O., Fielding, S. M., Marchetti, M. C. & Bi, D. Shear-driven solidification and nonlinear elasticity in epithelial tissues. *Phys. Rev. Lett.* **128**, 178001 (2022).
10. Hertaeg, M. J., Fielding, S. M. & Bi, D. Discontinuous shear thickening in biological tissue rheology. *Phys. Rev. X* **14**, 011027 (2024).
11. Lienkamp, S. S. et al. Vertebrate kidney tubules elongate using a planar cell polarity–dependent, rosette-based mechanism of convergent extension. *Nat. Genet.* **44**, 1382 (2012).
12. Etournay, R. et al. Interplay of cell dynamics and epithelial tension during morphogenesis of the *Drosophila* pupal wing. *eLife* **4**, e07090 (2015).
13. Heller, E., Kumar, K. V., Grill, S. W. & Fuchs, E. Forces generated by cell intercalation tow epidermal sheets in mammalian tissue morphogenesis. *Developmental Cell* **28**, 617–632 (2014).
14. Curran, S. et al. Myosin ii controls junction fluctuations to guide epithelial tissue ordering. *Developmental Cell* **43**, 480–492.e6 (2017).
15. Ruina, A. Slip instability and state variable friction laws. *J. Geophys. Res.: Solid Earth* **88**, 10359–10370 (1983).
16. Bak, P., Tang, C. & Wiesenfeld, K. Self-organized criticality: An explanation of the 1/f noise. *Phys. Rev. Lett.* **59**, 381 (1987).
17. Courcoubetis, G., Xu, C., Nuzhdin, S. V. & Haas, S. Avalanches during epithelial tissue growth; uniform growth and a drosophila eye disc model. *PLOS Computational Biol.* **18**, e1009952 (2022).
18. Prakash, V. N., Bull, M. S. & Prakash, M. Motility-induced fracture reveals a ductile-to-brittle crossover in a simple animal's epithelia. *Nat. Phys.* **17**, 504–511 (2021).
19. Popović, M., Druelle, V., Dye, N. A., Jülicher, F. & Wyart, M. Inferring the flow properties of epithelial tissues from their geometry. *N. J. Phys.* **23**, 033004 (2021).
20. Bi, D., Lopez, J. H., Schwarz, J. M. & Manning, M. L. A densityindependent rigidity transition in biological tissues. *Nat. Phys.* **11**, 10741079 (2015).
21. Bi, D., Yang, X., Marchetti, M. C. & Manning, M. L. Motility-driven glass and jamming transitions in biological tissues. *Phys. Rev. X* **6**, 021011 (2016).
22. O'Sullivan, M. J. et al. Irradiation induces epithelial cell unjamming. *Front. Cell Dev. Biol.* **8**, 21 (2020).
23. Falk, M. L. & Langer, J. S. Deformation and failure of amorphous, solidlike materials. *Annu. Rev. Condens. Matter Phys.* **2**, 353–373 (2011).
24. Manning, M. L. & Liu, A. J. Vibrational modes identify soft spots in a sheared disordered packing. *Phys. Rev. Lett.* **107**, 108302 (2011).
25. Patinet, S., Vandembroucq, D. & Falk, M. L. Connecting local yield stresses with plastic activity in amorphous solids. *Phys. Revi. Lett.* **117**, 045501 (2016).
26. Yang, H. et al. Multicell: geometric learning in multicellular development. *Preprint ArXiv* https://doi.org/10.48550/arXiv.2407.07055 (2024).
27. Staple, D. B. et al. Mechanics and remodelling of cell packings in epithelia. *Eur. Phys. J. E* **33**, 117–127 (2010).
28. Fielding, S. M., Cochran, J. O., Huang, J., Bi, D. & Marchetti, M. C. Constitutive model for the rheology of biological tissue. *Phys. Rev. E* **108**, L042602 (2023).

29. Bi, D., Zhang, J., Chakraborty, B. & Behringer, R. P. Jamming by shear. *Nature* **480**, 355–358 (2011).
30. Behringer, R. P. & Chakraborty, B. The physics of jamming for granular materials: a review. *Rep. Prog. Phys.* **82**, 012601 (2018).
31. Babu, V. & Sastry, S. Criticality and marginal stability of the shear jamming transition of frictionless soft spheres. *Phys. Rev. E* **105**, L042901 (2022).
32. Babu, V., Vinutha, H., Bi, D. & Sastry, S. Discontinuous rigidity transition associated with shear jamming in granular simulations. *Soft Matter* **19**, 9399–9404 (2023).
33. Shah, P., Arora, S. & Driscoll, M. M. Coexistence of solid and liquid phases in shear jammed colloidal drops. *Commun. Phys.* **5**, 222 (2022).
34. Morris, J. F. Shear thickening of concentrated suspensions: recent developments and relation to other phenomena. *Annu. Rev. Fluid Mech.* **52**, 121–144 (2020).
35. Sollich, P., Lequeux, F., Hébraud, P. & Cates, M. E. Rheology of soft glassy materials. *Phys. Rev. Lett.* **78**, 2020–2023 (1997).
36. Sollich, P. Rheological constitutive equation for a model of soft glassy materials. *Phys. Rev. E* **58**, 738–759 (1998).
37. Yin, G. & Solomon, M. J. Soft glassy rheology model applied to stress relaxation of a thermoreversible colloidal gel. *J. Rheol.* **52**, 785–800 (2008).
38. Bonn, D., Coussot, P., Huynh, H. T., Bertrand, F. & Debrégeas, G. Rheology of soft glassy materials. *Europhys. Lett. (EPL)* **59**, 786–792 (2002).
39. Mandadapu, K. K., Govindjee, S. & Mofrad, M. R. On the cytoskeleton and soft glassy rheology. *J. Biomech.* **41**, 1467–1478 (2008).
40. Bi, D. & Chakraborty, B. Rheology of granular materials: dynamics in a stress landscape. *Philos. Trans. R. Soc. A: Math., Phys. Eng. Sci.* **367**, 5073–5090 (2009).
41. Bi, D., Lopez, J. H., Schwarz, J. M. & Manning, M. L. Energy barriers and cell migration in densely packed tissues. *Soft Matter* **10**, 1885 (2014).
42. Samaniuk, J. R., Hermans, E., Verwijlen, T., Pauchard, V. & Vermant, J. Soft-glassy rheology of asphaltenes at liquid interfaces. *J. Dispers. Sci. Technol.* **36**, 1444–1451 (2015).
43. Chiou, K. K., Hufnagel, L. & Shraiman, B. I. Mechanical stress inference for two dimensional cell arrays. *PLoS Computational Biol.* **8**, e1002512 (2012).
44. Ishihara, S. & Sugimura, K. Bayesian inference of force dynamics during morphogenesis. *J. Theor. Biol.* **313**, 201–211 (2012).
45. Noll, N., Streichan, S. J. & Shraiman, B. I. Variational method for image-based inference of internal stress in epithelial tissues. *Phys. Rev. X.* **10**, 011072 (2020).
46. Ishihara, S. et al. Comparative study of non-invasive force and stress inference methods in tissue. *Eur. Phys. J. E* **36**, 1–13 (2013).
47. Kong, W. et al. Experimental validation of force inference in epithelia from cell to tissue scale. *Sci. Rep.* **9**, 14647 (2019).
48. Stanifer, E. & Manning, M. L. Avalanche dynamics in sheared athermal particle packings occurs via localized bursts predicted by unstable linear response. *Soft Matter* **18**, 2394–2406 (2022).
49. Richard, D., Elgailani, A., Vandembroucq, D., Manning, M. L. & Maloney, C. E. Mechanical excitation and marginal triggering during avalanches in sheared amorphous solids. *Phys. Rev. E* **107**, 034902 (2023).
50. Jaiswal, D., Moscato, Z., Tomizawa, Y., Claffey, K. P. & Hoshino, K. Elastography of multicellular spheroids using 3d light microscopy. *Biomed. Opt. Express* **10**, 2409–2418 (2019).
51. Falk, M. L. & Langer, J. S. Dynamics of viscoplastic deformation in amorphous solids. *Phys. Rev. E* **57**, 7192–7205 (1998).
52. Manning, M. L., Langer, J. S. & Carlson, J. M. Strain localization in a shear transformation zone model for amorphous solids. *Phys. Rev. E.* **76**, 056106 (2007).
53. Picard, G., Ajdari, A., Lequeux, F. & Bocquet, L. Elastic consequences of a single plastic event: a step towards the microscopic modeling of the flow of yield stress fluids. *Eur. Phys. J. E* **15**, 371–381 (2004).
54. Zhang, G., Ridout, S. A. & Liu, A. J. Interplay of rearrangements, strain, and local structure during avalanche propagation. *Phys. Rev. X* **11**, 041019 (2021).
55. Landau, L. D., Pitaevskii, L., Kosevich, A. M. & Lifshitz, E. M. *Theory of elasticity*. **7** (Elsevier, 1959).
56. Kawamura, H., Hatano, T., Kato, N., Biswas, S. & Chakrabarti, B. K. Statistical physics of fracture, friction, and earthquakes. *Rev. Mod. Phys.* **84**, 839–884 (2012).
57. Gutenberg, B. & Richter, C. F. Frequency of earthquakes in california. *Bull. Seismological Soc. Am.* **34**, 185–188 (1944).
58. Talamali, M., Petäjä, V., Vandembroucq, D. & Roux, S. Avalanches, precursors, and finite-size fluctuations in a mesoscopic model of amorphous plasticity. *Phys. Rev. E* **84**, 016115 (2011).
59. Karimi, K., Ferrero, E. E. & Barrat, J.-L. Inertia and universality of avalanche statistics: the case of slowly deformed amorphous solids. *Phys. Rev. E* **95**, 013003 (2017).
60. Amiri, A., Duclut, C., Jülicher, F. & Popović, M. Random traction yielding transition in epithelial tissues. *Phys. Rev. Lett.* **131**, 188401 (2023).
61. Lin, J. & Wyart, M. Mean-field description of plastic flow in amorphous solids. *Phys. Rev. X.* **6**, 011005 (2016).
62. Lin, J., Lerner, E., Rosso, A. & Wyart, M. Scaling description of the yielding transition in soft amorphous solids at zero temperature. *Proc. Natl Acad. Sci.* **111**, 14382–14387 (2014).
63. Lin, J., Saade, A., Lerner, E., Rosso, A. & Wyart, M. On the density of shear transformations in amorphous solids. *EPL (Europhys. Lett.)* **105**, 26003 (2014).
64. Richard, D., Kapteijns, G., Giannini, J. A., Manning, M. L. & Lerner, E. Simple and broadly applicable definition of shear transformation zones. *Phys. Rev. Lett.* **126**, 015501 (2021).
65. LANGER, J. Shear-transformation-zone theory of deformation in metallic glasses. *Scr. Materialia* **54**, 375–379 (2006).
66. Maloney, C. & Lemai^tre, A. Universal breakdown of elasticity at the onset of material failure. *Phys. Rev. Lett.* **93**, 195501 (2004).
67. Rottler, J., Schoenholz, S. S. & Liu, A. J. Predicting plasticity with soft vibrational modes: from dislocations to glasses. *Phys. Rev. E* **89**, 042304 (2014).
68. Ding, J., Patinet, S., Falk, M. L., Cheng, Y. & Ma, E. Soft spots and their structural signature in a metallic glass. *Proc. Natl Acad. Sci.* **111**, 14052–14056 (2014).
69. Xu, N., Vitelli, V., Liu, A. J. & Nagel, S. R. Anharmonic and quasi-localized vibrations in jammed solids–modes for mechanical failure. *EPL (Europhys. Lett.)* **90**, 56001 (2010).
70. Brito, C. & Wyart, M. Heterogeneous dynamics, marginal stability and soft modes in hard sphere glasses. *J. Stat. Mech.: Theory Exp.* **2007**, L08003–L08003 (2007).
71. Haase, K. & Pelling, A. E. Investigating cell mechanics with atomic force microscopy. *J. R. Soc. Interface* **12**, 20140970 (2015).
72. Bambardekar, K., Clément, R., Blanc, O., Chardès, C. & Lenne, P.-F. Direct laser manipulation reveals the mechanics of cell contacts in vivo. *Proc. Natl Acad. Sci.* **112**, 1416–1421 (2015).
73. Bonnet, I. et al. Mechanical state, material properties and continuous description of an epithelial tissue. *J. R. Soc. Interface* **9**, 2614–2623 (2012).
74. Fletcher, A. G., Osterfield, M., Baker, R. E. & Shvartsman, S. Y. Vertex models of epithelial morphogenesis. *Biophysical J.* **106**, 2291–2304 (2014).
75. Farhadifar, R., Röper, J.-C., Aigouy, B., Eaton, S. & Jülicher, F. The influence of cell mechanics, cell-cell interactions, and proliferation on epithelial packing. *Curr. Biol.* **17**, 2095–2104 (2007).

76. Lees, A. W. & Edwards, S. F. The computer study of transport processes under extreme conditions. *J. Phys. C: Solid State Phys.* **5**, 1921–1928 (1972).
77. Bitzek, E., Koskinen, P., Gähler, F., Moseler, M. & Gumbsch, P. Structural relaxation made simple. *Phys. Rev. Lett.* **97**, 170201 (2006).
78. Yang, X. et al. Correlating cell shape and cellular stress in motile confluent tissues. *Proc. Natl. Acad. Sci. USA* **114**, 12663–12668 (2017).
79. Maloney, C. E. & Lemai^tre, A. Amorphous systems in athermal, quasistatic shear. *Phys. Rev. E* **74**, 016118 (2006).
80. Li, X., Das, A. & Bi, D. Mechanical heterogeneity in tissues promotes rigidity and controls cellular invasion. *Phys. Rev. Lett.* **123**, 058101 (2019).
81. Huang, J., Nguyen, A. Q. & Bi, D. jxhuangphys/sheared_voronoi_model: shear_voronoi_matlab_v25.02.21 https://doi.org/10.5281/zenodo.14907889 (2025).

Acknowledgements

We thank Craig E. Maloney, Marko Popović, and Jie Lin for insightful discussions. We acknowledge support from the National Science Foundation (grant nos. DMR-2046683 and PHY-2019745), the Alfred P. Sloan Foundation, the Human Frontier Science Program (Ref.-No.: RGP0007/2022), the NIGMS of the National Institutes of Health (NIH) under award number R35GM15049, and the Northeastern University Discovery Cluster.

Author contributions

All authors contributed to the research design. A.Q.N. and J.H. performed and analyzed the numerical simulations with guidance from D.B. The manuscript was written by A.Q.N. and D.B., with input from J.H.

Competing interests

The authors declare no competing interests.

Additional information

Supplementary information The online version contains supplementary material available at https://doi.org/10.1038/s41467-025-58526-7.

Correspondence and requests for materials should be addressed to Dapeng Bi.

Peer review information *Nature Communications* thanks the anonymous reviewer(s) for their contribution to the peer review of this work. A peer review file is available.